Published by IOP Publishing for Sissa Medialab

Received: *January 31, 2020*
Accepted: *February 25, 2020*
Published: *April 6, 2020*

Plasma Physics by Laser and Applications (PPLA 2019)
Physics Department, University of Pisa, Pisa, Italy
29–31 October, 2019

2020 JINST 15 C04018

Ultra-fast laser machining of stainless steel

G. Lazzini,[a] **A.H.A. Lutey,**[a] **L. Romoli,**[a] **M. Allegrini**[b,c] **and F. Fuso**[b]

[a] *Department of Engineering and Architecture, University of Parma, via delle Scienze 181/a, 43124 Parma, Italy*
[b] *Dipartimento di Fisica "Enrico Fermi", Università di Pisa, Largo Bruno Pontecorvo 3, 56127 Pisa, Italy*
[c] *CNR-NANO, Largo Bruno Pontecorvo 3, 56127 Pisa, Italy*

E-mail: gianmarco.lazzini@unipr.it

Abstract: Ultra-fast laser machining is emerging as an effective tool for modifying surface morphology in many technological fields. The process entails laser ablation, which in turn involves complex interplay between phenomena pertaining to laser matter interaction, thermo-physical effects, ionisation and material expansion, amongst others. In addition, the transient formation of surface plasmon polaritons and subsequent interaction with the impinging radiation can lead to quasi-periodic surface structures, in particular when metals or semiconductors are used. In the present paper, stainless steel is machined with the goal of producing smooth surfaces. Nonetheless, as demonstrated by highly sensitive scanning probe surface diagnostics, texturing is achieved at multiple length scales. Mechanisms leading to the observed surface features are proposed and the relationship with process parameters briefly discussed.

Keywords: Manufacturing; High-power fiber lasers

[1]Corresponding author.

https://doi.org/10.1088/1748-0221/15/04/C04018

Contents

2020 JINST 15 C04018

1 Introduction

A key factor in the attempt to modify surface properties such as wetting, scattering of radiation or particles, and tribological or antibacterial behaviour foresees tuning the surface roughness in order to obtain tailored characteristics. Within this context, laser texturing has emerged as a promising and effective approach [1] to modulate the surface topography leading to a wealth of surface structures. Several technological strengths can be attributed to laser machining such as its effectiveness in modifying various materials, the possibility to operate on planar or curved surfaces, the single-step character of the process and the ability to perform irradiation in air.

The development of ultra-fast laser sources capable of emitting pulses with sub-ps duration and the consequent availability of increasingly efficient laser facilities has opened up new scenarios for the exploitation of physical and chemical phenomena involved in laser matter interaction. The minimal duration of ultra-short laser pulses prevents energy transfer processes via electron-phonon coupling. This in turn limits material melting and the consequent formation and redeposition of melted material and droplets around the irradiated area. In technological applications such as drilling, cutting, milling and welding, the above mentioned feature reduces the Heat Affected Zone (HAZ), the region where solid material is modified either chemically or in terms of microstructure due to temperature increases, thus enhancing machining precision [2].

Depending on the process parameters employed, ultra-fast laser machined substrates can exhibit laser-induced surface features that vary over a broad range of sizes, from the nano- to the micro-scale, often referred to as hierarchical surfaces. These have stimulated growing interest owing to their similarities with biological surfaces, which possess functional properties of appeal in view of advanced applications including antibacterial treatments and biomedical sensing [3–5].

Although several models have been proposed to describe laser processing, basic mechanisms ruling the interplay between ablation and texturing are still far from being completely understood, in particular when machining entails repeated irradiation by multiple spatially overlapping laser pulses, as is customary in industrial applications. In this paper we present examples of surface textures achieved with ultrashort pulses on stainless steel along with their morphological investigation.

2 Ultra-fast laser texturing

The set of physical phenomena giving rise to laser-induced structures occurs at fluences similar or slightly above the single shot ablation threshold, the energy density leading to measurable material removal, typically ranging from fractions of J/cm^2 to a few J/cm^2 [6, 7]. Upon arrival of the laser pulse, electrons in the target absorb energy within a skin layer whose thickness is in the range of tens of nm depending on the laser wavelength and optical properties of the target. In the case of metals, the process entails direct excitation of electrons in the conduction band, whilst in semiconductors and dielectrics additional processes are involved such as interband transitions induced by non-linear effects, multiphoton absorption, tunnelling, and avalanche ionisation [8]. Absorption takes place on a time scale dictated by the characteristic time needed by the electron Fermi distribution to relax, typically in the range of a few fs [9]. Since thermalisation with the lattice takes place over a much longer time scale governed by electron-phonon coupling, the ultra-fast nature of the laser hampers efficient exchange of energy with the lattice during irradiation. The evolution of the resulting non equilibrium system can be described in terms of the so-called two-temperature model [9]. This picture treats temporal evolution of electron and lattice temperatures in terms of coupled non-linear differential equations depending on thermodynamic parameters, e.g., electron and phonon heat capacities and relaxation times. In metals and semiconductors, generally showing high thermal conductivities, the heating rate of the irradiated target can reach values of up to 10^{14} K/s [10]. Due to such rapid heating, portions of the irradiated target can suddenly reach metastable conditions such as superheated liquid and material can be ejected through vaporisation, non-thermal melting, fragmentation and other processes. At low fluence, a spallation regime is established where the acoustic wave generated by laser-induced pressure leads to the formation of voids of depth $\sim$ 100 nm. With increasing laser fluence, void domains tend to coalesce leading to detachment of material layers that are tens of nm thick [11] and consequent rapid expulsion of a mixture of vapour and droplets containing charged particles created both during and immediately after laser absorption.

Within such a complex frame, one of the most striking features of ultra-fast laser machining is the possibility to obtain controlled topographical modifications of the irradiated substrate in the form of Laser Induced Periodic Surface Structures (LIPSS). These structures represent a quasi-periodic modulation of the surface topography leading to arrays of ripples or dots depending on laser polarisation and other process parameters [12]. Two major types of LIPSS have been identified [13], denoted as Low and High Spatial Frequency LIPSS (LSFL and HSFL, respectively). These differ according to spacing (in the range $\lambda/2 - \lambda$ for LSFL, with λ the laser wavelength, and $< \lambda/2$ for HSFL) and orientation (mostly orthogonal for LSFL and parallel for HSFL). In the case of LSFL on metals, where a large density of surface charge occurs, excitation of Surface Plasmon Polaritons (SPP) and the subsequent interference with the incoming radiation are involved [13], resulting in the spacing being affected by the angle of incidence. Under such conditions, the space-dependent (periodic) laser energy distribution is "imprinted" onto the material giving rise to quasi-periodic texturing of the machined surface. Determining the robustness of this process during its evolution is a topic that is still under debate [14] and involves accounting for all above mentioned phenomena ruling material ablation. For instance, it is known that hydrodynamic effects in the metastable layers can play a role at high fluence, coalescing smaller structures into large bumps [15].

2020 JINST 15 C04018

3 Experimental

Samples used for machining experiments were AISI 316L stainless steel plates with a residual roughness of $R_a \sim 0.2 - 0.3$ μm. This low carbon alloy was chosen for its widespread application in industrial contexts due to its wear and corrosion resistance. A fibre laser source (Raydiance Starfemto R-100) was employed for processing, delivering 800 fs pulses at a wavelength of 1552 nm, a maximum pulse energy of 50 μJ and repetition rate of 100 kHz. The source was equipped with a 3-D beam scanning head (Arges Precession Elephant) producing a spot which could be moved on the substrate along computer controlled circular trajectories with a maximum radius of 0.5 mm and a nominal spatial resolution of 0.1 μm at an adjustable tangential speed. For the samples considered in the present paper, the laser path followed a spiral-like trajectory with the number of turns set within the range $N_{\text{turn}} = 6 - 96$ and an outer diameter of 600 μm. Laser polarisation was circular, controlled through a set of wave-plates. The distance between objective and substrate could be adjusted in a ± 1 mm range: examples considered in the present paper have been machined in "in-focus" conditions corresponding to an approximately Gaussian laser intensity distribution on the surface with nominal diameter of 20 μm. Figure 1(a) reports a sketch of the laser machining apparatus, while figure 1(b) presents an example of the machined surfaces.

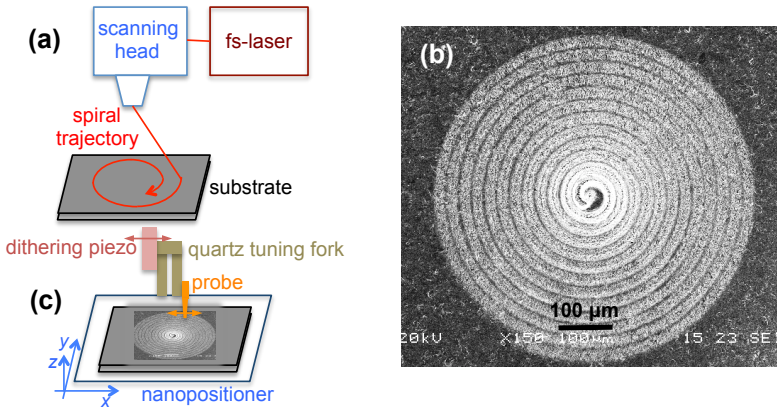

Figure 1. Sketch of the laser machining apparatus (a); a SEM image of a stainless steel sample machined with $N_{\text{turn}} = 12$ (b); sketch of the ShFM head (c). Schematics are not to scale.

Further to scanning electron microscopy (SEM), surface topography was acquired via a specifically conceived scanning probe technique denoted as Shear Force Microscopy (ShFM) [16], see figure 1(c). The custom setup employed a 3-axis closed-loop nanopositioner (Physik Instrumente 517.3) able to displace the sample with an accuracy of 1 nm and 0.1 nm and maximum travel of 100 μm and 20 μm in the in-plane (x, y) and vertical (z) directions, respectively. The probe consisted of a 125 μm diameter tungsten wire, electrochemically etched to an apex diameter below 50 nm. The probe was glued onto the prong of a commercial quartz tuning fork, which enabled conversion of the oscillation amplitude into an electrical signal. The whole assembly was kept in oscillation by a dithering piezo-actuator at a frequency close to the mechanical resonance of the system (around 32 kHz) and an amplitude of a few nm. Thanks to the dithering geometry, oscillation was aligned parallel to the surface, preventing accidental contact between the tip and surface and therefore

2020 JINST 15 C04018

enabling true non-contact operation. As a consequence, negligible wear was produced on the tip while surface scratches or other damage were prevented during the scan.

When the tip approached the surface at typical distances of a few nm, the oscillation was significantly damped because of the friction created by the air layer trapped between the tip and surface. The demodulated electrical signal was sent to a feedback loop employed to maintain the tip-to-sample distance constant by acting on the z-displacement of the nanopositioner. The resulting correction signal, acquired point-by-point during a raster scan of the surface, led to calibrated topography maps. Moreover, dephasing between the dithering and oscillation signals measured by a digital dual lock-in amplifier (Stanford Research Systems SR830) was simultaneously acquired. Since the phase of a forced mechanical oscillator is extremely sensitive to variations in friction and therefore tip-to-sample distance in the applied setup, the acquired phase maps enabled features corresponding to small height variations to be effectively highlighted.

4 Results and discussion

The present paper reports experiments whose main goal was to demonstrate laser ablation as an effective approach for milling stainless steel surfaces in industrial-oriented applications [17]. From a technological point of view, such a non-contact and unobtrusive process could be highly relevant in precision machining. Milling requires the energy supplied by the laser to be homogeneously distributed over the entire machined surface in order to reduce its roughness, therefore minimising the height of the obtained texture. To this end, specific laser scanning strategies were deployed such as the spiral path, where the laser spot was moved at a constant tangential speed of 110 mm/s. Owing to the high repetition rate, subsequent laser spots were separated by 1.1 μm, corresponding to a tangential spatial overlap of around 95%. The pulse energy was set to 10 μJ, leading to a nominal fluence of $\Phi_L \simeq 3.2$ J/cm^2, higher than the threshold $\Phi_{thr} \simeq 0.13$ J/cm^2 reported for Ti:Sa laser ablation of stainless steel [7]. As already pointed out, the chosen process parameters, resulting in significant ablation depths (up to tens of nm per pulse [17]) and massive material ejection, were not expected to promote LIPSS while giving rise to hydrodynamic processes eventually leading to texturing on larger length scales.

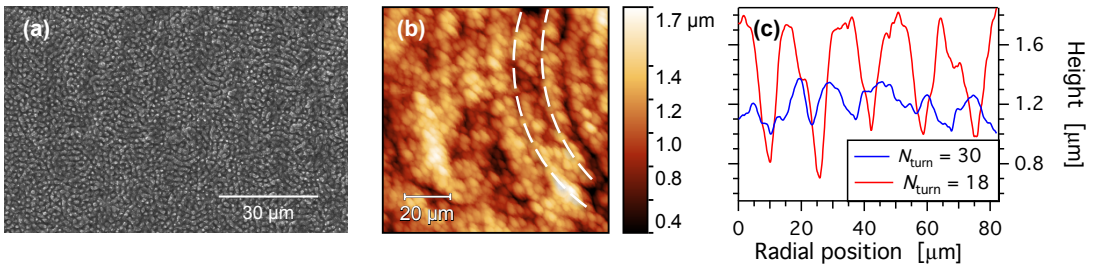

Figure 2. SEM image (a) and ShFM topography map (b) of a stainless steel sample machined with the parameters outlined in the text ($N_{turn} = 30$); representative line profiles along the radial direction of the spiral trajectories for samples produced with $N_{turn} = 30$ and 18 (c). The dashed lines in panel (b) represent the approximate trajectory of the laser spot in two subsequent turns of the machined spiral. Note that different portions of the same sample are shown in the panels (a) and (b).

2020 JINST 15 C04018

Figure 2 reports a SEM image and a ShFM topography map [panels (a) and (b), respectively] of a laser machined substrate. In this example, $N_{\text{turn}} = 30$ leading to a radial spatial overlap of 50% between successive laser passes. In combination with the chosen fluence, which was well above the ablation threshold, such conditions led to a relatively smooth surface. The average roughness as acquired on the considered map was $S_a = 167$ nm. Portions of the spiral trajectory taken by the laser beam were detected, in particular in the ShFM map. An example is highlighted by the dashed lines in figure 2(b), where the lower local height reflected the stronger local laser intensity close to the centre of the Gaussian spot. Further to a few higher protrusions and deeper valleys or holes, the topography map exhibited a relatively dense texture of small dots or bubbles, with micrometer-sized lateral dimensions and height in the order of a few hundred nm. The shape of such features was elongated in a direction approximately orthogonal to the laser scanning path. The same features appeared differently shaped in the SEM image due to the different contrast mechanism and nonlinear dependence on topography. This suggests that the orientation and elongated shape were not constant over the entire machined surface, possibly due to material inhomogeneities. Surface texturing achieved under such conditions was a combination of predefined structures and those directly related to laser scanning with a dense distribution of dot-like features.

When the number of turns was reduced, resulting in lower radial overlap of the laser scanning path, the occurrence of individual, separate grooves could be detected on the surface. This is confirmed by figure 2(c), where line profiles along the radial direction of the spiral-like path are reported for samples produced with $N_{\text{turn}} = 30$ and 18. Figure 3 shows the topography [panels (a–c)] and corresponding phase maps [panels (d–f)] acquired on a sample machined with $N_{\text{turn}} = 18$, corresponding to a radial overlap below 20%. The largest ShFM scan area, shown in panel (a), shows the outermost $4-5$ turns of the machined spiral and a portion of the non-machined surface at the bottom-right of the map. Grooves with a typical depth of $\sim 0.5-0.8$ μm were evident, resulting from insufficient radial overlap for efficient super-positioning of ablation effects. The resulting roughness of the displayed map was $S_a = 288$ nm. It must be noted that partial overlap of the laser scanning path also produced partial redeposition of ablated material along groove borders. This was highlighted by the fact that the full width at half maximum of the grooves (typically $7-8$ μm) was smaller than the nominal laser spot diameter, while the average groove depth was lower than the expected ablation depth at the applied fluence [17]. Other interesting features were revealed in small area scans. Figure 3(b) shows elongated structures oriented along the diagonal of the map, roughly corresponding to the tangential laser scanning direction. As the features were very small in height, low contrast was achieved in the topography map. High contrast was instead attained in the phase maps, as in the region enclosed within the dashed ellipse in figure 3(e). Typical spacing of such structures was found to be below 1 μm, in agreement with expectations for LIPSS. These were found to be distributed on the surface of samples produced with low radial super-positioning, mostly aligned with the tangential laser scanning direction and located close to groove borders, in regions where the effective laser fluence could be estimated in the range $0.3-0.8$ J/cm^2.

Due to the circular polarisation of laser pulses, quasi-periodic surface structures were expected to be produced in the form of dot-like LSFL [12, 13]. However, the laser angle of incidence was not always normal due to the effects of previously fired laser pulses. As a consequence, absorption of the TM and TE components was anisotropic, eventually leading to conditions similar to those experienced in laser ablation with elliptical polarisation [18], hence the occurrence of ripple-like LSFL. Remarkably, such structures were mostly found along groove borders, where a larger

2020 JINST 15 C04018

surface slope was found and the major axis of the effective elliptical polarisation was approximately orthogonal to the laser scanning direction. It must be noted that similar ripple-like structures could not be discerned at the bottom of the grooves. This was confirmed by small area ShFM scans centred within the grooves such as those shown in figure 3(c) and (f). In this case, the high sensitivity of ShFM phase maps allowed detection of morphological structures with straight edges, which could be ascribed to the grain borders of stainless steel. In other words, ablation within the vicinity of the laser axis and centre of the Gaussian intensity distribution led to almost flat surfaces with residual texturing due to the microstructure of the substrate material.

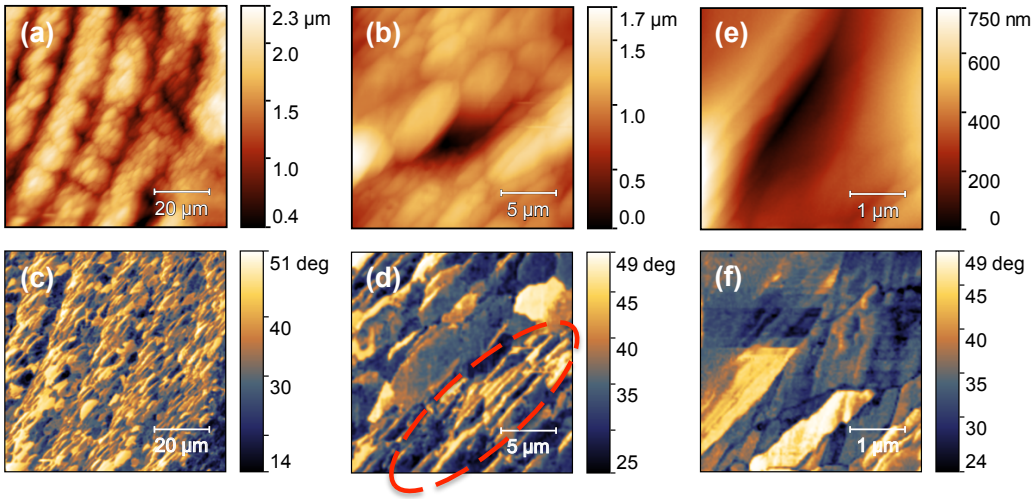

Figure 3. ShFM topography (a–c) and phase (d–f) maps of a stainless steel sample machined with the parameters outline in the text (N_{turn} = 18). Different portions of the same sample are shown in panels corresponding to different scan areas. The colour scale of phase maps is calibrated in units of dephasing referenced to the measurement for free oscillations of the tip. The dashed ellipse in panel (d) highlights features associated with ripple-like LIPSS.

5 Conclusions

Ultra-fast laser machining of stainless steel in a configuration aimed at surface milling with multiple laser pulses above the ablation threshold revealed the presence of surface features characterised by various length scales ranging from macroscopic effects similar in size to the laser spot diameter, to dot and ripple-like LIPSS, and microstructural features. Thanks to the use of highly sensitive surface diagnostics enabled by ShFM, each class of detected feature could be associated with relevant topography variations.

Whilst the goal of the presented approach was to develop a machining process aimed at minimising roughness in the milled regions and therefore reducing unwanted texturing, the inherently complex interplay between different phenomena involved in laser ablation led to surface texturing. On one hand, this can hamper utilisation of ultra-fast laser machining as a production tool for flat and smooth surfaces. On the other, however, the proven ability to achieve micro- and nano-sized surface features depending on process parameters paves the way for advanced applications such as chemical-free and durable antibacterial surfaces. To this end, further efforts will be devoted to better disentangle the role of each process parameter.

2020 JINST 15 C04018

References

[1] A.Y. Vorobyev and C. Guo, *Direct femtosecond laser surface nano/microstructuring and its applications*, *Laser Photonics Rev.* **7** (2012) 385.

[2] B.N. Chichkov, C. Momma, S. Nolte, F. Alvensleben and A. Tünnermann, *Femtosecond, picosecond and nanosecond laser ablation of solids*, *Appl. Phys.* **A 63** (1996) 109.

[3] E. Skoulas, A. Manousaki, C. Fotakis and E. Stratakis, *Biomimetic surface structuring using cylindrical vector femtosecond laser beams*, *Sci. Rep.* **7** (2017) 45114.

[4] A.H.A. Lutey et al., *Towards laser-textured antibacterial surfaces*, *Sci. Rep.* **8** (2018) 10112.

[5] CMS collaboration, *Simulation of the dynamic inefficiency of the CMS pixel detector*, 2015 *JINST* **10** C05006 [arXiv:1411.6770].

[6] J. Byskov-Nielsen, J.-M. Savolainen, M.S. Christensen and P. Balling, *Ultra-short pulse laser ablation of metals: threshold fluence, incubation coefficient and ablation rates*, *Appl. Phys.* **A 101** (2010) 97.

[7] D. Pietroy, Y.D. Maio, B. Moine, E. Baubeau and E. Audouard, *Femtosecond laser volume ablation rate and threshold measurements by differential weighing*, *Opt. Expr.* **20** (2012) 29900.

[8] J. Reif, *Basic physics of femtosecond laser ablation*, in *Laser-surface interactions for new materials production*, A. Miotello and P.M. Ossi eds., Springer, Berlin, Heidelberg, Germany (2010).

[9] S.I. Anisimov et al., *Electron emission from metal surfaces exposed to ultrashort laser pulses*, *Zh. Eksp. Teor. Fiz.* **66** (1974) 375 [*JETP* **39** (1974) 375].

[10] C. Wu, M.S. Christensen, J.-M. Savolainen, P. Balling and L.V. Zhigilei, *Generation of subsurface voids and a nanocrystalline surface layer in femtosecond laser irradiation of a single-crystal Ag target*, *Phys. Rev.* **B 91** (2015) 035413.

[11] M.E. Povarnitsyn, T.E. Itina, M. Sentis, K.V. Khishchenko and P.R. Levashov, *Material decomposition mechanisms in femtosecond laser interactions with metals*, *Phys. Rev.* **B 75** (2007) 235414.

[12] J. Bonse, J. Krüger, S. Höhm and A. Rosenfeld, *Femtosecond laser-induced periodic surface structures*, *J. Laser Appl.* **24** (2012) 042006.

[13] J. Bonse, S. Höhm, S.V. Kirner, A. Rosenfeld and J. Krüger, *Laser-induced periodic surface structures — a scientific evergreen*, *IEEE J. Select. Topics Quantum Electron.* **23** (2017) 9000615.

[14] X. Sedao et al., *Growth twinning and generation of high-frequency surface nanostructures in ultrafast laser-induced transient melting and resolidification*, *ACS Nano* **10** (2016) 6995.

[15] G.D. Tsibidis, C. Fotakis and E. Stratakis, *From ripples to spikes: a hydrodynamical mechanism to interpret femtosecond laser-induced self-assembled structures*, *Phys. Rev.* **B 92** (2015) 041405.

[16] F. Tantussi et al., *Shear-force microscopy investigation of roughness and shape of micro-fabricated holes*, *Precis. Eng.* **41** (2015) 32.

[17] L. Romoli, F. Tantussi and F. Fuso, *Laser milling of martensitic stainless steels using spiral trajectories*, *Opt. Lasers Eng.* **91** (2017) 160.

[18] G. Lazzini, L. Romoli, F. Tantussi and F. Fuso, *Nanostructure patterns on stainless-steel upon ultrafast laser ablation with circular polarization*, *Opt. Laser Technol.* **107** (2018) 435.

2020 JINST 15 C04018